Ion kinetic transport in the presence of collisions and electric field in TJ-II ECRH plasmas

2007 Plasma Phys. Control. Fusion 49 753

(http://iopscience.iop.org/0741-3335/49/6/005)

IOP PUBLISHING PLASMA PHYSICS AND CONTROLLED FUSION

Plasma Phys. Control. Fusion **49** (2007) 753–776 doi:10.1088/0741-3335/49/6/005

Ion kinetic transport in the presence of collisions and electric field in TJ-II ECRH plasmas

F Castejón[1,4], L A Fernández[2,4], J Guasp[1], V Martin-Mayor[2,4], A Tarancón[3,4] and J L Velasco[3,4]

[1] Laboratorio Nacional de Fusión—Asociación Euratom/Ciemat, Madrid-28040, Spain
[2] Departamento de Física Teórica I. Universidad Complutense de Madrid, Madrid-28040, Spain
[3] Departamento de Física Teórica. Universidad de Zaragoza, Zaragoza-50009, Spain
[4] BIFI: Instituto de Biocomputación y Física de Sistemas Complejos, Zaragoza-50009, Spain

E-mail: francisco.castejon@ciemat.es

Received 6 November 2006, in final form 22 March 2007
Published 27 April 2007
Online at stacks.iop.org/PPCF/49/753

Abstract

The ion collisional transport is estimated for the TJ-II device without the assumption of radially narrow particle trajectories, which is usually made in neoclassical transport studies. One million particles are followed in a realistic TJ-II magnetic configuration, taking into account collisions and the electric field. Global features of transport, not present in the customary neoclassical models, appear. The main results reached by considering the actual particle geometries are the monotonic increasing of heat and particle fluxes with minor radius, the non-diffusive character of transport, the appearance of asymmetries on the magnetic surfaces and the non-Maxwellian character of the distribution function.

1. Introduction

The study of ion trajectories in low collisionality plasmas is very important both for tokamaks and for stellarators. Several issues make this study useful to understand the confinement in those devices. Some instances are the kinetic transport and the behaviour of particles in a given magnetic configuration; the confinement of fast ions and alpha particles (see e.g. [1, 2]); the evaluation of direct losses and the effect of the magnetic ripple on particle confinement, not only in stellarators but also in tokamaks [3,4]. The trajectories of particles have been estimated in stellarators since a long time ago as a first assessment of the confinement properties of a given magnetic configuration (see e.g. [5]), but this kind of work is less common in tokamaks. A thorough study of the trajectories of particles confined in a tokamak can be found in [6].

TJ-II is a medium size flexible heliac ($R = 1.5\,\mathrm{m}$, $a < 0.22\,\mathrm{m}$) characterized by a complex magnetic configuration [7] (see also figure A1), which complicates transport studies. The customary neoclassical transport estimates assume that the transport coefficients depend only on the local plasma characteristics, namely the magnetic structure, the local electric field

and the collisionality. This hypothesis is equivalent to the assumption that the typical size of the trajectories performed in a collision time is small. However, due to the TJ-II magnetic configuration, some ion particle orbits include large radial excursions in a single collision time. Indeed, these excursions can be of the order of or wider than the characteristic gradient lengths of the density, temperature and electrostatic potential. The very same particle, depending on its velocity, could visit plasma regions of widely differing conditions, which casts doubt on the local approximation. For instance, the drift kinetic equation solver (DKES) code [8], which is the most common neoclassical transport tool, presents the limitation that the neoclassical transport coefficients for TJ-II are affected by large error bars in the low collisionality regime, which is the most relevant in ECRH core plasmas. Therefore, this code cannot be used as such for studying the neoclassical transport properties of TJ-II ECRH plasmas. Some approximations relying on the use of a simplified geometry of the magnetic configuration have been developed [9], but their validity should be checked.

To overcome these difficulties, a Monte Carlo method has been successfully used to estimate the diagonal coefficients of the neoclassical transport matrix [10]. These coefficients do not present the same uncertainties as those obtained by using DKES, but the local diffusive transport hypothesis is still assumed, together with the average on every magnetic surface. The contribution of large banana orbits cannot be included in this code, since the diffusion coefficient is assumed to be local, i.e. it only depends on the characteristics of a single point in TJ-II, and the flux is assumed to be diffusive.

In a previous work [11], the transport properties were estimated by launching a large number of ions (typically 10^7) and following their trajectories during approximately two collision times. In that work, the possibility of particle collisions was not taken into account because the emphasis was made on the effects of an electric field profile at short times. In this way, the influence of the background magnetic and electric fields on the kinetic transport could be investigated. In the absence of collisions, only limited physical consequences could be extracted from the results presented there. Nevertheless, a clear conclusion of such estimates is that the characteristic radial width of orbits in a single collision time is large and, hence, the electric field, the magnetic structure and the collisionality vary along the trajectory of the particle, making the local approximation doubtful. Therefore, global plasma characteristics must be taken into account in more accurate transport estimates for TJ-II. In fact, a recent perturbative computation of the distribution function has shown [12] that the usual diffusive transport approach does not work in TJ-II.

In this work, we improve over the study in [11] by considering ion (proton) collisions, by using the Langevin approach [13] to follow the trajectories of a large number of ions (typically 10^6) in realistic TJ-II ECRH plasmas. Generally speaking, the Langevin approach offers a number of new possibilities. To start with, it is ideally suited for massive parallel computations, both in supercomputer facilities and in computing grids. It is fairly easy to generalize adding stochastic terms or dealing with different geometries (envisaged applications include electron–ion interactions, plasma heating and ripple effects in tokamaks). It allows for interesting insights; for instance, the here found asymmetries and inhomogeneities on every magnetic surface (see section 6.2) were not predicted in previous theoretical work performed by the usual methods. And, indeed, the Langevin approach does not need the assumptions of small particle orbits or diffusive transport. Furthermore, although the customary methods for neoclassical transport estimates are at work, it is always useful to obtain the results by different methods, in order to compare the validity of the involved hypothesis.

The here used Langevin method and collision operator, see appendix A, were already used by Boozer and Kuo–Petravic [13], and are usual in this kind of works [14]. The main novelty of this work is the extension of the Boozer–Kuo Petravic approach to the complex

magnetic configurations found in the stellarator TJ-II. Our implementation differs from [13] only in technical details. For instance, we use a numerical scheme to integrate the underlying stochastic differential equations which is appropriate for a magnetic configuration interpolated from tabulated values (see below). Moreover, we are able to follow, for the first time in the TJ-II device, particle trajectories for a time comparable to the discharge duration. The large number of trajectories, as well as a careful data analysis (see appendix C), allow us to obtain accurate estimates of the time evolution of, for instance, the profile of the particle and energy fluxes or the kinetic energy profile.

Important transport consequences can be extracted from the properties of the trajectories of particles: the particle and heat fluxes are shown to be non-diffusive and to rise along the minor radius. This transport calculation approach yields non-negligible toroidal and poloidal asymmetries, because it does not need to average on every magnetic surface. In particular, the up/down fluxes are different, and inhomogeneous distributions of particles along the toroidal and poloidal angles are observed on every magnetic surface.

The remainder of this paper is organized as follows: section 2 is devoted to the description of the conditions of our plasma and the lack of validity of the local ansatz in several regions of the plasma. Section 3 describes the model used for these studies. Section 4 is devoted to studying the persistence of particles. Section 5 presents the behaviour of the global ion heat and particle fluxes, while some features of global transport that do not appear in the customary transport studies are shown in section 6. The conclusions are presented in section 7. Three appendices are added at the end of the paper: appendix A shows the collision operator that is used in these studies, the choice of the numeric algorithm is discussed in appendix B, while appendix C is devoted to showing how the TJ-II geometry is considered to calculate the fluxes.

2. TJ-II conditions for the simulation

The typical TJ-II ECRH plasmas, heated by microwaves at the second harmonic of the electron-cyclotron resonance frequency, are characterized by a high electron temperature and low density, limited by the cut-off. The electron–ion collisions, the only mechanism for ion heating in these plasmas, are therefore rare. Hence, the ion temperature is low, about $\sim$100 eV or even lower, with a temperature profile, taken from charge exchange (CX) measurements, and it is almost flat [15]. The electron density is low, with a hollow profile (figure 1—bottom). The potential profile is taken similar to those obtained by heavy ion beam probe (HIBP) measurements and presents a minimum around $\rho \approx 0.7$ (figure 1—top). Here, $\rho = \sqrt{\phi/\phi_0}$ is the normalized radial coordinate, while ϕ and ϕ_0 are the magnetic fluxes through the local and the last closed magnetic surfaces. This electrostatic potential is the experimental one and should be the result of the ambipolarity condition plus the diamagnetic effect. The latter is small for this low plasma pressure; the former implies that the electron flux should compensate the ion flux in the steady state. Therefore, the final value of the potential depends on both the ion and the electron fluxes, the latter are not considered in this work.

The characteristic ion–ion collision frequency is still pretty low due to the low density, despite the fact that the ion temperature is not high. The typical values of ion–ion collision time in these TJ-II plasmas are $\tau_c = 2.7 \times 10^{-4}$ s in the centre of the plasma and $\tau_c = 1.1 \times 10^{-3}$ s at $\rho = 0.7$. In order to evaluate the collisional regime (low, plateau or Pfirsch–Schlüter) of these plasmas, these collision times must be compared with the bounce time, as it has been done in [10]. But, willing to elucidate the validity of the usual neoclassical approaches (which consider that transport coefficients only depend on local plasma characteristics), this time scale must also be compared with the typical time for a particle to drift radially. In section 6.1, a

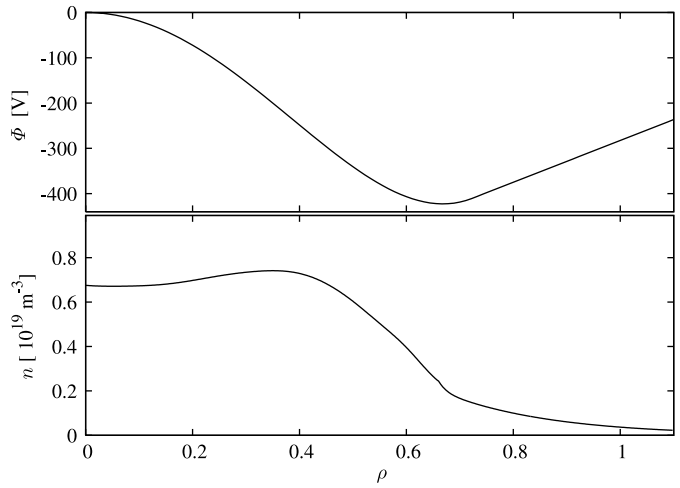

Figure 1. (Top) Profile of electric potential used in this work. (Bottom) Profile of particle density in our plasma.

radial drift time of $\tau_r \approx 5 \times 10^{-3}$ s is estimated. It is only one order of magnitude larger than the collision time, which means that the local calculations are still accurate in the plasma centre but are doubtful close to the plasma edge.

To make the above statements more precise, we compare in figure 2 the typical size of the radial excursions with the relevant length-scales of our plasma (see the following sections for details on the calculation). The calculated orbit sizes, defined as $\Delta\rho(t) = \langle(\rho(t) - \rho(0))^2\rangle^{1/2}$, are shown in figure 2—left with and without electric field. The trajectories start at several radial positions with velocities distributed according to a Maxwellian (thus, with a uniform distribution of the pitch). The calculated orbit width is lowered by the electric field, which is not surprising. In a collision time, the calculated sizes reach 20% of the plasma minor radius in the case without field. In the presence of electric field, the width of the orbits in the centre of the plasma lies between 5% and 10% of the minor radius for $t \sim 10^{-4}$ s, and between 10% and 15% for $t \sim 10^{-3}$ s. This is also to be compared (see figure 2—right) with the gradient lengths of the different quantities that have an influence on confinement: for the density, we have $L_n \equiv |n/(\partial n/\partial\rho)| \sim 0.2$ in a wide region (ρ between 0.4 and 0.7) of the plasma, similar to the average orbit size. The same happens with the gradient of the electric potential, whose characteristic length is described by $L_\Phi \equiv |(\Phi - \Phi_{\min})/(\partial\Phi/\partial\rho)|$. In terms of the magnetic field, the quantity $L_B \equiv |B/(\partial B/\partial\rho)|$, although highly non-uniform, is of the order of the macroscopic size of the device. Therefore orbits can be wider or of the order of the gradient lengths of density and electric potential in the zones of strongly varying density (between $\rho \approx 0.4$ and $\rho \approx 0.7$) and electric potential (between $\rho \approx 0.4$ and $\rho \approx 0.8$), where the particle suffers different collisionalities and electric field along its trajectory. This makes at best doubtful the local ansatz in several regions of the plasma.

3. The ion dynamics

3.1. The guiding-centre drift approximation

The well-known guiding-centre approximation allows one to disentangle the fast gyromotion from the relatively slow displacement of the particle along the device. Instead of

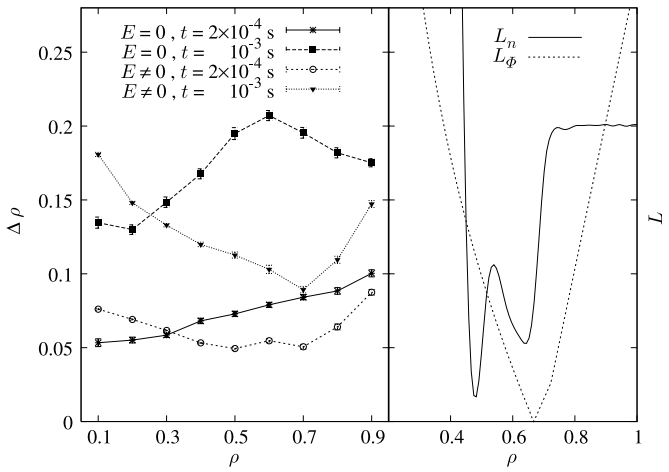

Figure 2. (Left) Orbit sizes, with and without electric field, for trajectories starting at several radial positions. The times shown, $t = 2 \times 10^{-4}$ s and $t = 10^{-3}$ s, are approximately the collision times in the centre and in the edge of the plasma, respectively. (Right) Characteristic length-scales L of the plasma versus ρ, as obtained from the gradients of the density and the potential profiles.

the position and velocity of the physical particle, $\vec{r}$ and $\vec{v}$, one considers the position and velocity of the guiding centre of its fast Larmor precession, namely $\vec{r}_{\rm GC}$ and $\vec{u}$. Of course, $\vec{B}(\vec{r}_{\rm GC}) \cdot \vec{v} = \vec{B}(\vec{r}_{\rm GC}) \cdot \vec{u}$ (i.e. the motion along the magnetic field lines is the same for the physical particle and for its guiding centre). We then reduce the six-dimensional dynamical problem with variables $\{\vec{r}, \vec{v}\}$ to a basically equivalent five-dimensional problem with variables $\{\vec{r}_{\rm GC}, u_\parallel, v^2\}$ ($v^2 \equiv \vec{v} \cdot \vec{v}$ rather than u^2, as we want to track the kinetic energy of the physical particle). Actually, for technical convenience we shall use the *pitch*, λ, and the particle kinetic energy, $\frac{1}{2}mv^2$, in units of the thermal energy of the background field particles (m is the mass of the ions):

$$x^2 \equiv \frac{v^2}{v_{\rm th}^2}, \qquad v_{\rm th} = \sqrt{\frac{2kT}{m}}, \qquad \lambda \equiv \frac{u_\parallel}{\sqrt{v^2}}. \tag{1}$$

We recall that the range of variation for these variables is $-1 \leqslant \lambda \leqslant 1$ and $0 \leqslant x^2 < \infty$.

Then, one obtains a closed set of dynamical equations for $\{\vec{r}_{\rm GC}, \lambda, x^2\}$, where the electric charge is $+e$, the drift velocity is $\vec{v}_{\rm d}$, the magnetic moment of the physical particle is μ and $x \equiv +\sqrt{x^2}$:

$$\frac{{\rm d}\vec{r}_{\rm GC}}{{\rm d}t} \equiv \vec{a}_{r_{\rm GC}} \equiv \vec{u} = v_{\rm th} x \lambda \frac{\vec{B}}{B} + \vec{v}_{\rm d}, \tag{2}$$

$$\vec{v}_{\rm d} = \frac{\vec{E} \times \vec{B}}{B^2} + \frac{m x^2 v_{\rm th}^2 (1+\lambda^2)}{2eB^3} (\vec{B} \times \vec{\nabla} B), \tag{3}$$

$$\mu = \frac{m x^2 v_{\rm th}^2 (1-\lambda^2)}{2B}, \tag{4}$$

$$\frac{{\rm d}x^2}{{\rm d}t} \equiv a_{x^2} = \frac{2e}{m v_{\rm th}^2} (\vec{E}_\perp \cdot \vec{v}_{\rm d}), \tag{5}$$

$$\frac{{\rm d}\lambda}{{\rm d}t} \equiv a_\lambda = -\frac{\mu}{m x v_{\rm th}} (\vec{\nabla} B)_\parallel - \frac{e\lambda}{m x^2 v_{\rm th}^2} (\vec{E}_\perp \cdot \vec{v}_{\rm d}). \tag{6}$$

In TJ-II, as in the the usual stellarator operation, $E_\parallel = 0$ is fulfilled, since no current is driven by external coils. These equations describe the motion of the guiding centre in the absence of particle collisions.

3.2. The Monte Carlo method

When one considers collisions, the Boltzmann equation formalism [13] (see also appendix A) yields a Fokker–Planck-like equation for the five-dimensional phase-space distribution function, $f(t, \vec{r}_{GC}, \lambda, x^2)$:

$$\frac{\partial f}{\partial t} + \vec{\nabla}_{r_{GC}} \cdot (\vec{u} f) + \frac{\partial}{\partial \lambda}(a_\lambda f) + \frac{\partial}{\partial x^2}(a_{x^2} f) = \mathcal{L} f. \tag{7}$$

In equation (7), $\mathcal{L}$ is a second-order differential operator, whose explicit form can be found in equation (A.7), that represents collisions to the Boltzmann level of accuracy (i.e. disregarding pair correlation functions). In spite of its appearance, equation (7) is not linear, as it depends on local features of the plasma, such as the particle density and the local temperatures, through the collision rates ν_d and ν_E (see appendix A). To linearize it, we follow the common practice [6, 13] of neglecting the effects of the diffusive particles on the collision rates. In other words, we will be dealing with *test particles* moving in (and colliding with) a stationary *field* particle distribution. The latter is described by experimentally fixed density, temperature and electrostatic potential profiles. This first approximation is already rather computationally demanding and actually represents the state of the art [6]. However, it provides very interesting information, as shown below.

Once it is understood that f is the distribution function of the test particles, so rendering equation (7) linear in f, we may interpret this equation as a standard Fokker–Planck equation (see e.g. [18–21]). It is well known that an equivalence exists between a Fokker–Planck equation with constant diffusion coefficients and a Langevin equation. This equivalence may be extended to general diffusion equations, with variable diffusion coefficients, thanks to the advent of Itô calculus [18, 19]. In our case, equation (7) is equivalent to a set of five coupled (Itô) stochastic differential equations:

$$\frac{\mathrm{d}\vec{r}_{GC}}{\mathrm{d}t} = \vec{a}_{r_{GC}}, \tag{8}$$

$$\frac{\mathrm{d}\lambda}{\mathrm{d}t} = [a_\lambda + a_\lambda^{\mathrm{Ito}}] + b_\lambda \xi_\lambda, \tag{9}$$

$$\frac{\mathrm{d}x^2}{\mathrm{d}t} = [a_{x^2} + a_{x^2}^{\mathrm{Ito}}] + b_{x^2} \xi_{x^2}. \tag{10}$$

In equations (9) and (10), ξ_λ and ξ_{x^2} are independent *white noises* [18, 19]. The functions a_λ, a_λ^{Ito}, a_{x^2}, $a_{x^2}^{\mathrm{Ito}}$, b_λ, b_{x^2} depend on the local density and temperature, as well as on $\vec{r}_{GC}$, λ and x^2. Their detailed functional dependence can be found in equations (2)–(6) and appendix A.

Equations (8)–(10) represent an Itô diffusion process [18] in a five-dimensional space. Therefore, if the positions and velocities of the diffusive particles at time t_0 are distributed with a probability density proportional to $f(t_0, \vec{r}_{GC}, \lambda, x^2)$, the probability density of their position and velocities at time t will be proportional to the solution of equation (7), $f(t, \vec{r}_{GC}, \lambda, x^2)$. Note that, due to the linearity of equation (7), the normalization of f is arbitrary. If we are to use it as a probability density it will be normalized to 1, while it will be normalized to the total number of particles if it is to be considered a distribution function.

In this work we have chosen the probability distribution for the starting positions and velocities of the diffusive test ions according to the underlying field particle distribution, that

is assumed to be Maxwellian in the kinetic energy (comments about the integration measure for $f(t, \vec{r}_{GC}, \lambda, x^2)$ are given in appendix A):

$$f(t_0, \vec{r}_{GC}, \lambda, x^2) = n(\vec{r}_{GC}) \frac{x\, e^{-x^2}}{\sqrt{\pi}}, \tag{11}$$

where $n(\vec{r}_{GC})$ is the number density of the physical particles, that is assumed to be identical to that of their guiding centres. We have introduced a Maxwellian distribution function only for the kinetic energy rather than for the whole mechanical energy of the particle, i.e. we have taken equation (11) instead of

$$f(t_0, \vec{r}_{GC}, \lambda, x^2) = \frac{\mathcal{N}}{Z} \frac{x\, e^{-x^2 - e\Phi(\vec{r}_{GC})/kT}}{\sqrt{\pi}}, \tag{12}$$

where Z is the configurational partition function and $\mathcal{N}$ is the total number of physical particles. The initial condition in equation (11) ensures that we can estimate the evolution of the set of particles under the action of an electric field, including the time scale for reaching an equilibrium with the background. In this way, it is possible to explore the collective phenomena that are driven by the electric field. The non-stationary behaviour observed in the flux evolution is therefore a collective effect due to the fact that the distribution function is not the equilibrium one. The problem could be understood as the evolution of ions after having changed the electrostatic potential profile. Electrons can be considered adiabatic and with such a dynamics that compensates the background ion flux in order to keep the net charge flux zero. The ion temperature of the field particles and the density and electric potential profiles are taken similar to the experimental ones (see section 2).

Particles are lost when they collide with the groove of the vacuum chamber that protects the central TJ-II conductor or with the walls of the vacuum chamber. This means that we may calculate the *sinks* where particles escape from the plasma. Since the distribution function is essentially stationary during the discharge, this is actually a computation of the rhythm at which particles need to be injected in the plasma.

The algorithm actually used to solve the Itô stochastic differential equation (Itô SDE), equations (8)–(10), is sometimes baroquely named [6, 22] *Monte Carlo operator*. One should be aware that, once the Fokker–Planck operator and the conditions of the background field particles are chosen, there is a huge freedom on the choice of the algorithm [18, 19, 21, 23, 24]. This choice is a matter of simplicity and efficiency, there is no physics involved, because all algorithms solve the same Fokker–Planck equation.

In the TJ-II case, we are hampered by the complexity of the magnetic geometry, which is not written in analytical form but it is tabulated in a grid [16]. This grid fits the magnetic surfaces in the real space and does not need to assume nested magnetic surfaces [16, 17], although no magnetic islands or ergodic zones are considered for the moment. We therefore have to interpolate the coefficient functions as needed in the integration. From the computational point of view, this is actually a problem: usual manipulations (such as a change of variables or the choice of stochastic calculus) yield different results if the magnetic field is interpolated from a grid. In appendix B we present seemingly redundant computations that would be identical for an analytically known magnetic configuration, but that allow us to estimate the systematic errors induced by the discretization in a grid.

For the time being, let us simply say that in this problem there are five significant time scales: the period of the oscillatory motion of a trapped particle in a banana orbit ($\sim 10^{-5}$ s), the time needed to complete a cycle around TJ-II ($\sim 10^{-4}$ s), the collision time ($\sim 10^{-4}$–10^{-3} s) the time of accumulation of ions close to the minimum of the potential ($\sim 10^{-3}$–10^{-2} s) (see figure 9) and the typical exit time due to collisions with the groove

or the vacuum chamber (∼0.03 s). We follow the particle trajectories for times up to a tenth of a second. We have limited ourselves to 0.1 s in order to describe the stationary part of the TJ-II pulse, which lasts about 0.3 s. This disparity in scales makes the simplest first algorithm, the Euler algorithm [18], useless. A more sophisticated algorithm (appendix B) was needed to reduce the time-discretization errors with a reasonable computer effort.

In summary, we have developed a computer code that solves the guiding-centre equations in the presence of collisions. We name it ISDEP (Integrator of Stochastic Differential Equations for Plasmas).

4. The persistence of particles

Among the many possibilities opened by a particle description of the plasma, the most straightforward one is the ion confinement study. One may even envisage a detailed study of the frequency and location of the particles impacts with the walls of the chamber or with the central coil. However, this study would be sensitive to changes in the magnetic geometry far from the magnetic axis. Unfortunately, the grid we are using [16] is not accurate beyond $\rho = 1.1$, and this study will be delayed to the near future. In this work we make only a global study of the persistence of the particles.

We define the persistence up to time t, $\mathcal{P}(t)$, as the fraction of trajectories that remain in the plasma at time t. A trajectory ends either when the particle impacts the chamber walls or the coil, or when it goes beyond $\rho = 1.5$. We have checked that changing the ending criterion to $\rho = 1.1$ changes τ less than 3%. However, some particles are able to reenter the $\rho < 1.1$ region (that is correctly sampled by our grid), producing perfectly reasonable trajectories. We thus prefer to consider that only particles going so far away as $\rho = 1.5$ inevitably leave the plasma. Although this is a somehow arbitrary choice, we have checked that its effects on all computed quantities are smaller than for τ.

In figure 3 we show $\mathcal{P}(t)$ both with and without radial electric field. In TJ-II the field is indeed present. Yet, our computer experiment allows us to quantify the importance of the electric field in preventing the particles from leaving the plasma. To do that, we have fitted the time evolution by an exponential decay ($\mathcal{P}(t) \propto \mathrm{e}^{-t/\tau}$), although it is not purely exponential: at short times, some curvature is observed for $t < 0.02$ s. Hence, fitting to a purely exponential from $t = 0.0075$ s on, we find:

$$\tau_{E=0} = 0.0090(1)\ \mathrm{s}, \qquad \tau_{E\neq 0} = 0.0286(1)\ \mathrm{s}. \tag{13}$$

We thus conclude that the electric field extends the ion confinement duration by roughly a factor of three. As expected, the radial electric field tends to improve the plasma confinement. These results can be compared with the experimental particle confinement time of 21(3) ms [25] for similar conditions.

5. The behaviour of global fluxes

The evolution of the average effective radius of all the particles shows that, in the presence of collisions, ions tend to accumulate close to the minimum of the potential. In figure 4 we plot the evolution of the radial ion distribution. We also show the electrostatic potential profile as a function of the normalized effective radius. Note that the characteristic time scale of the accumulation process (∼10^{-4}–10^{-3} s) is imposed by the dynamics of the macroscopic problem and did not appear by considering the microscopic dynamics (see section 3.2).

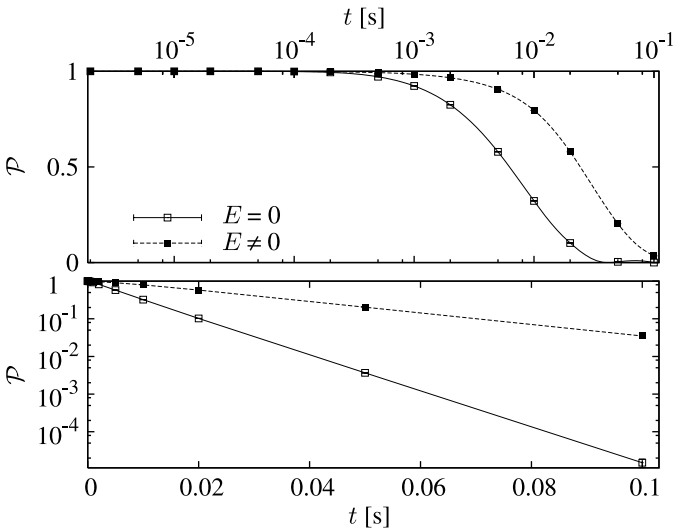

Figure 3. Persistence of particles as a function of time. In the top part we plot the persistence versus the logarithm of time. In the bottom part, the logarithm of the persistence is plotted versus time in linear scale, to make evident the exponential decay at long times. The error bars are plotted but they are so small that they are visible only for the last times.

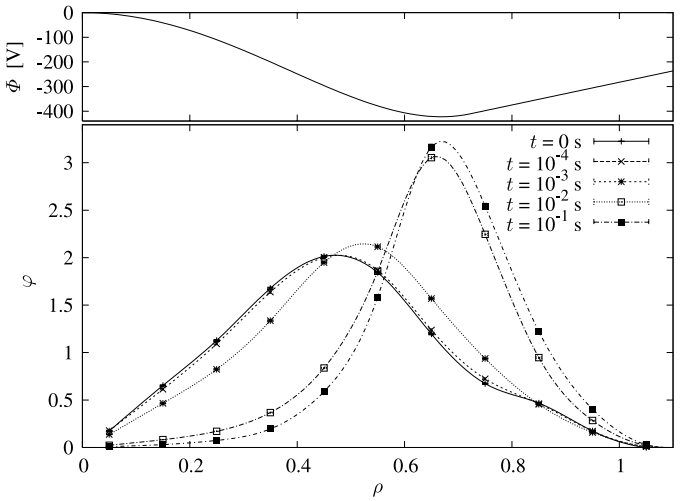

Figure 4. Electrostatic potential profile as a function of the radial coordinate (up) and normalized radial ion distribution $\varphi(\rho)$ for selected times (down). When comparing with figure 1, keep in mind that $\varphi(\rho) \propto \rho\, n(\rho)$.

A more detailed insight can be obtained by studying the radial flux of particles and energy integrated over the magnetic surface S, by means of the following velocity and surface integrals:

$$\Gamma(\rho) = \int_S \int_0^\infty \mathrm{d}\, x^2 \int_{-1}^{1} \mathrm{d}\,\lambda\; f(\vec{r}_{\mathrm{GC}}, \lambda, x^2)\; \vec{u} \cdot \mathrm{d}\vec{S}, \tag{14}$$

$$q(\rho) = \int_S \int_0^\infty \mathrm{d}\, x^2 \int_{-1}^{1} \mathrm{d}\,\lambda\; f(\vec{r}_{\mathrm{GC}}, \lambda, x^2) \left(\frac{1}{2} m v^2\right) \vec{u} \cdot \mathrm{d}\vec{S}. \tag{15}$$

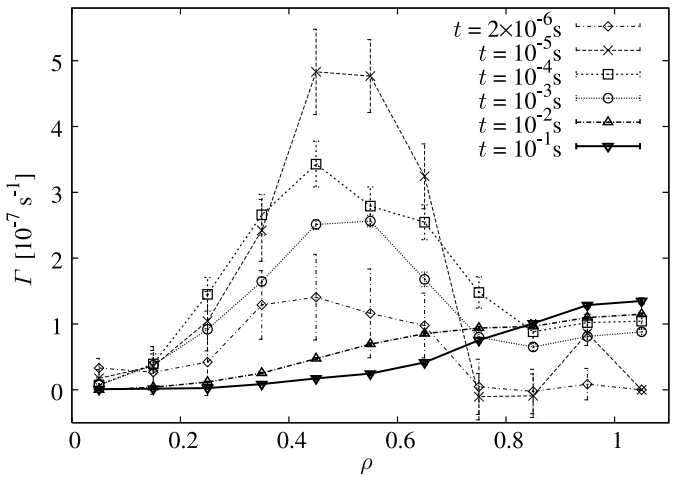

Figure 5. Radial flux of particles in the plasma as a function of the radial coordinate for several selected times. The curves are normalized dividing by the total number of remaining ions in the plasma.

We transform these expressions into volume integrals over each radial corona (the number of coronas considered is 11). The calculational method, that has allowed us to significantly reduce errors, is explained in appendix C.

Figures 5 and 6 show, respectively, the particle and the energy fluxes integrated on every magnetic surface. For a broad range of time, 10^{-6} s $< t < 10^{-2}$ s, there is a wide maximum in the $0.4 < \rho < 0.7$ region: the ions drift to the minimum of the potential. Since both figures show the same qualitative behaviour, it seems that all the ions, no matter its kinetic energy, are affected by the field. Although the most energetic particles will be less sensitive to the effect of the electric field, the differences between both the heat and the particle fluxes are small because the height of the minimum of the plasma potential is about 400 eV, several times the mean kinetic energy of ions. This experimental potential profile is determined both by the ion and the electron fluxes, which explains why it can be larger than the average ion kinetic energy.

For greater times, the flux profiles become monotonic, increasing as we get close to the edge. This is related to the process of particle redistribution along the radius together with escapes, which occur mostly at relatively long times. Note that, even though the density profile evolves during the simulation, its qualitative shape remains the same, with a maximum of low varying position and width. However the flux profiles differ completely, showing a clear monotonic increase with ρ in the stationary late phase.

For the sake of clarity, the detailed time evolution of the particle radial flux is shown in figure 7 for two different magnetic surfaces that are representative of the full plasma section. Note that, at early times, 10^{-5} s $< t < 10^{-4}$ s, a number of particles accumulate at the edge of the plasma, since no important ion escape has occurred yet (see figure 3). For times of the order of 10^{-2} s $< t < 10^{-1}$ s, we observe in figure 7 that the fluxes become time independent. Under the action of the electric field, the plasma has reached a steady state, in equilibrium with the field particles (note that the time scale coincides with that of the last paragraph of section 3.2). Thus, the estimated fluxes for those late times can be understood as the ones that are present in TJ-II stationary conditions, and this method is valid for estimating the transient and the steady conditions, of course, as far as the error bars allow one to be confident of the results.

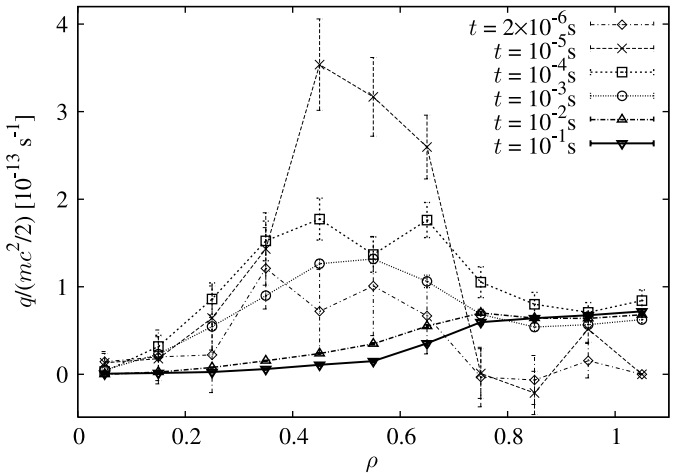

Figure 6. Radial flux of energy in the plasma as a function of the radial coordinate for several selected times. Normalization as in figure 5.

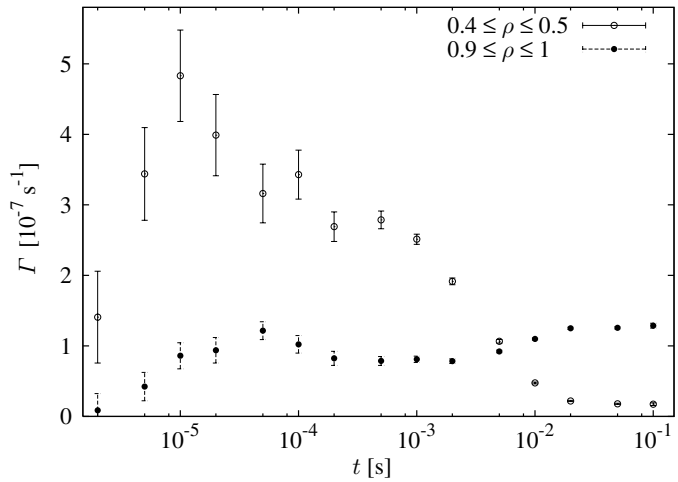

Figure 7. Radial flux of particles in the plasma as a function of time for two different radial intervals.

Now consider the toroidal flux through a corona S_C inside a toroidal slab:

$$\Gamma_\phi(\rho) = \int_{S_C}\int_0^\infty \mathrm{d}\,x^2 \int_{-1}^{1} \mathrm{d}\,\lambda\; f(\vec{r}_{GC}, \lambda, x^2)\; \vec{u}\cdot\mathrm{d}\vec{S} \tag{16}$$

$$= \int_{S_C}\int_0^\infty \mathrm{d}\,x^2 \int_{-1}^{1} \mathrm{d}\,\lambda\; f(\vec{r}_{GC}, \lambda, x^2)\; u_\phi \mathrm{d}S. \tag{17}$$

We want to estimate the average of this quantity over the toroidal angle. We thus measure the average toroidal velocity of the particles that are in each radial corona, which is proportional to the flux (see appendix C).

Figure 8 shows the toroidal flux as a function of the radial coordinate. For $\rho < 0.8$, the flux remains roughly null during all the simulated time. Nevertheless, a non-zero flux appears

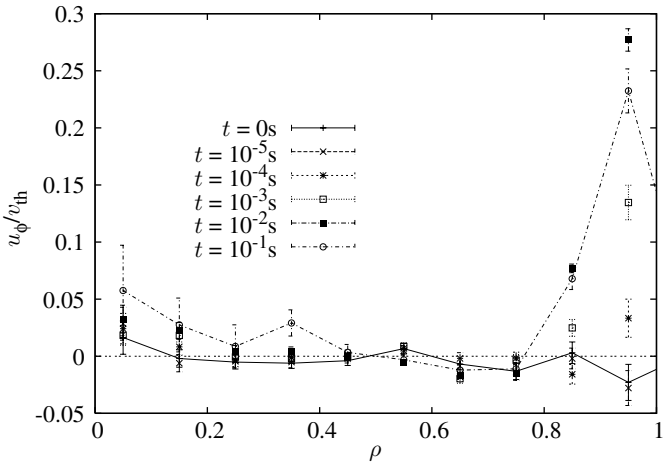

Figure 8. Average toroidal velocity of ions at the plasma as a function of the radial coordinate for selected times. For the sake of clarity, lines join the points only for the two extremal times. Recall that $v_{th} = \sqrt{2kT/m}$.

for $\rho > 0.8$ and $t > 10^{-4}$ s. At that time, looking at figures 3 and 9, one sees that few particles have escaped yet and that a non-negligible portion of the plasma is in the external region. Thus, integrating to the whole plasma, we obtain a net toroidal current. In [11], in the absence of collisions, the toroidal flux was found to be zero in every magnetic surface. Hence, collisions must play a crucial role in the origin of this current, together with the existence of an ion pressure gradient, similarly to how the bootstrap current is generated.

6. Features of global transport

6.1. Non-diffusive behaviour

As discussed in section 2, the present calculation does not assume a diffusive transport. Non-diffusive features can then appear in this computer experiment. We saw in section 5 (figure 4) that ions tend to accumulate close to the minimum of the potential. In figure 9 we show the time evolution of the average and the variance of ρ of the ions present in the plasma. If transport were diffusive, we would expect the variance of the radial coordinate to have a linear evolution in time, $\mathrm{var}(\rho) \sim t$. This seems to be true for early times, $t < 10^{-3}$ s, but for longer times there is a clearly non-diffusive behaviour while particles accumulate close to the minimum of the electrostatic potential. Moreover, one can fit the time evolution of the average ρ to $\langle\rho\rangle = \rho_f + (\rho_0 - \rho_f)e^{-t/\tau}$, finding an exponential approximation to stationarity from ρ_0 to ρ_f. We obtain a characteristic accumulation time of $\tau \sim 5 \times 10^{-3}$ s.

The evolution of $\rho(t)$ gives us also the time scale of radial drift of the particles, which is $\tau_r = 5 \times 10^{-3}$ s, as shown above. The customary neoclassical ordering, in which the typical drift time is much larger than the collision time, implies that the radial excursions of the particles in a single collision time are small, in such a way that the plasma characteristics that the particle comes across are almost constant. In our case, although the drift time is larger than the collision one, the neoclassical ordering is not always fulfilled in the plasma and some global effects can appear. The collision time in the centre of the device ($\approx 10^{-4}$ s) is smaller than the drift time in a factor 20. Nevertheless, in the edge of the device both quantities are

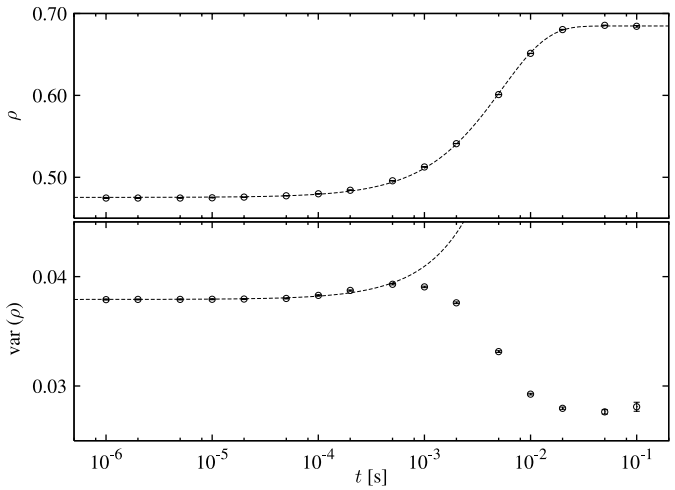

Figure 9. Average (up) and variance (down) of the radial coordinate ρ as a function of time. The lines are exponential (up) and linear (down) fits of the corresponding data points.

of the same order. This means that the change of plasma characteristics along the trajectory must be taken into account. Moreover, the typical drift velocities in the edge are larger than those in the centre.

6.2. Asymmetries

The complexity of the magnetic configuration and the non-local transport are the origin of several non-negligible up/down, toroidal and poloidal asymmetries. Some of these asymmetries have been observed experimentally [26].

In particular, the difference between the up/down fluxes leads to different densities of particles in the upper and lower half of the device. Figure 10 shows the time evolution of the average z-coordinate of the ions. Starting with an approximately equal amount of ions at each half of the device, $\langle z \rangle$ decreases monotonically at early times and immediately separates from zero. Nevertheless, for $10^{-5}\,\mathrm{s} < t < 10^{-3}\,\mathrm{s}$, the proportion of up/down ions remains nearly constant. In the same interval (see figure 7), there is a broad maximum in the flux at medium ρ, when the ions are being attracted towards the minimum of the potential, so the electric field has a clear symmetrizing effect. The time evolution of $\langle z \rangle$ in the absence of an electric field supports this affirmation: the proportion of up ions decreases almost monotonically with no plateau.

We define a new poloidal angle to be $\theta = \chi - 4\phi$, in order to take into consideration the TJ-II geometry. χ is the usual poloidal angle and ϕ the toroidal one. Now, $\theta = \pi$ always corresponds to the groove region. Figure 11 shows the evolution of the poloidal distribution of ions. The profiles are normalized by the initial value, thus taking into account the volume in real space of the different θ intervals. For $t > 5 \times 10^{-3}\,\mathrm{s}$, there is a slight but non-negligible accumulation of particles in the vicinity of the groove. This happens for the times when the ions losses become important, and is due to the specific structure of the TJ-II magnetic field.

The component of velocity parallel to the magnetic field, integrated to the whole plasma, appears to be toroidally asymmetric. Since the initial velocity distribution is Maxwellian, it must be zero at the beginning. Figure 12 shows its time evolution: it decreases monotonically

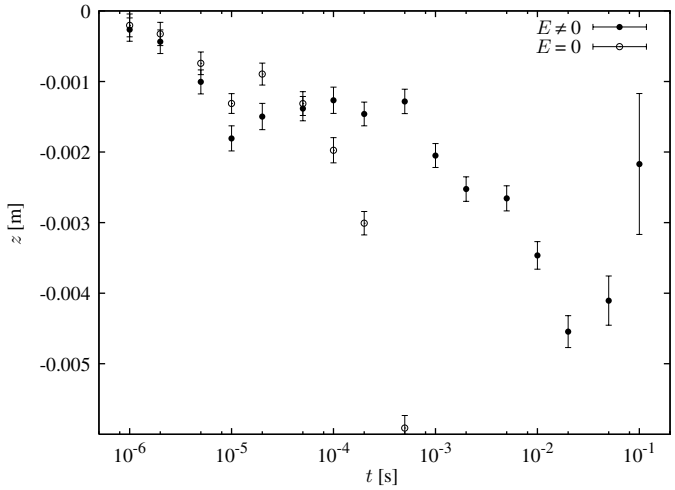

Figure 10. Average z-coordinate of ions at the plasma as a function of time.

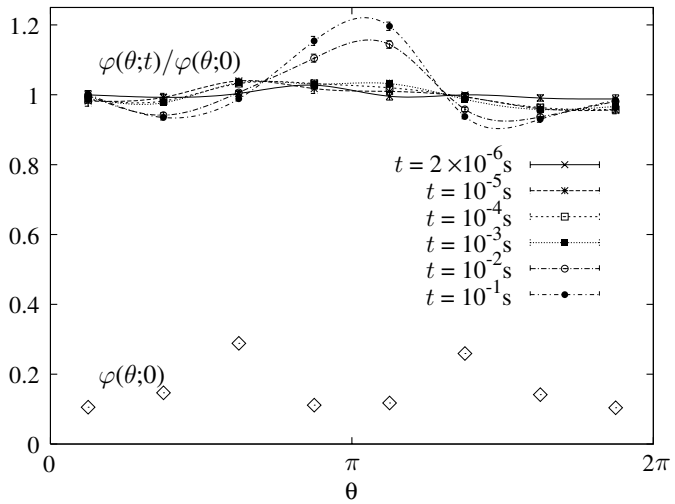

Figure 11. Poloidal ion distribution $\varphi(\theta; t)$ for several selected times as a function of the poloidal coordinate. The initial profile, $\varphi(\theta; 0)$, was taken as the normalization for later times.

from zero due to the effect of the collisions and the ion pressure gradient, showing the development of a negative ion current (see section 5).

Reference [26] shows the qualitative agreement of the up/down and poloidal asymmetries presented here with those measured by arrays of soft x-ray detectors and bolometers. Beyond that charge exchange (CX) spectroscopy should also detect these effects. The flux of neutrals measured by the neutral particle analyser has to be different when the instrument is facing at upper and lower positions with respect to the equatorial plane. The up/down asymmetry is mainly due to the $\vec{B} \times \vec{\nabla} B$ term in the drift kinetic equation that tends to push particles in a preferred direction. The neutral flux detected by the CX spectrometer should be more intense in the lower positions of TJ-II. The accumulation of ions close to the groove of TJ-II, as

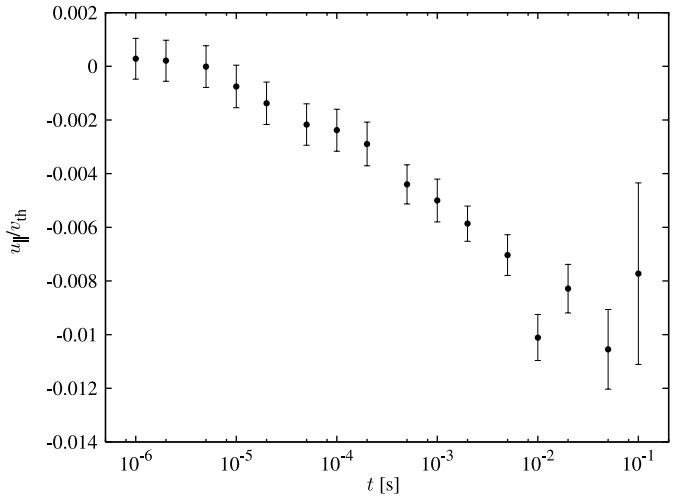

Figure 12. Average parallel velocity of ions at the plasma as a function of time.

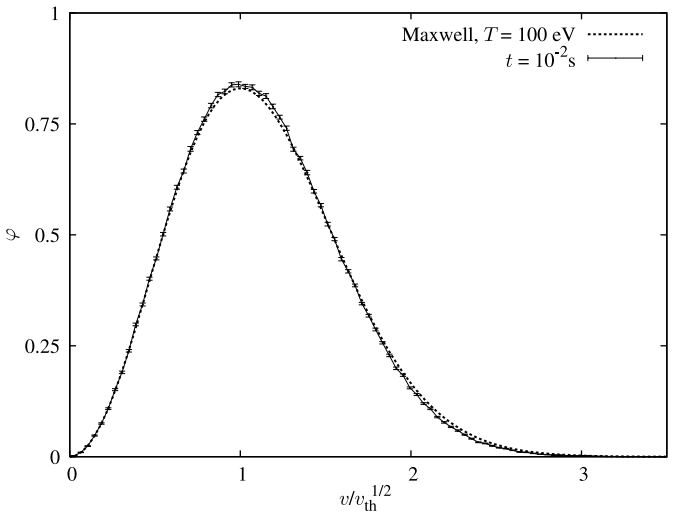

Figure 13. Distribution function of the physical velocity of the particles $\varphi(v/v_{th})$ (normalized to unit), after 10^{-2} s. This distribution is an integral over the full spatial extension of the plasma. For comparison, we also plot the starting distribution, that is exactly Maxwellian.

seen in figure 11, should imply that the measurements of the neutral flux performed along a chord crossing such a poloidal angle must be larger than any other. Moreover, the neutral flux depends on the convolution along a chord of the ion and neutral particle densities, and the latter must be larger close to the plasma at these positions.

6.3. The selective losing of particles

As expected, the distribution function for the kinetic energy (integrated to the full spatial extension of the plasma), is more similar to the Maxwellian than in the collisionless regime [11], even at long times (see figure 13). However, we note that the difference with the Maxwellian

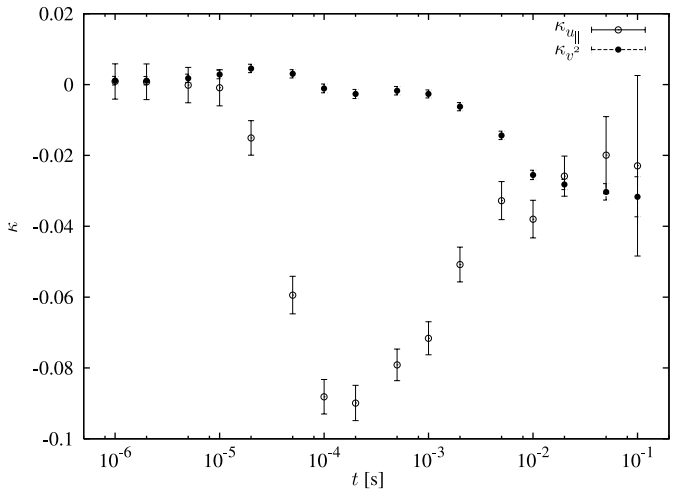

Figure 14. Cumulants defined in equation (18) as a function of time.

is largest at high velocities, which is not surprising, since the fast particles are more easily lost. To make this statement quantitatively precise, we introduce the generalized cumulants for the parallel velocity $u_\parallel$ and the particles velocity v^2:

$$\kappa_{u_\parallel} = \frac{\langle u_\parallel^4 \rangle}{\langle u_\parallel^2 \rangle^2} - 3, \qquad \kappa_{v^2} = \frac{\langle v^4 \rangle}{\langle v^2 \rangle^2} - \frac{5}{3}. \tag{18}$$

The cumulants are dimensionless ratios of mean values; they are exactly zero for a Maxwellian distribution (irrespective of temperature). A negative (positive) value indicates a lack (excess) of high-energy particles with respect to the Maxwellian. As shown in figure 14, the deviations from the zero value are small at all times. However, with our statistical accuracy they are clearly negative from 10^{-5} s for $\kappa_{u_\parallel}$ and from 10^{-4} s for κ_{v^2}. Note that the time evolution of $\kappa_{u_\parallel}$ has two characteristic scales: deviations from Maxwellianity are clearly measurable from 10^{-5} s, as indicated by the strong decrease. However, at the characteristic time scale for collisions (10^{-3}–10^{-4} s) the trend changes and the cumulant again approaches Maxwellianity. The difference between the two cumulants shows a preferred losing of particles with high parallel velocity. At any rate, the two dimensionless ratios, $\kappa_{u_\parallel}$ and κ_{v^2}, are consistent with a selective (and small) losing of particles: the ions starting with a higher kinetic energy are more likely to escape earlier.

6.4. Dynamics of the ion temperature profile

In a previous experimental work [15], the perpendicular measurement of ion spectra at three different radial positions (corresponding to $\rho \approx 0.6$, 0.9 and 1.1) was shown. It was observed that such spectra were almost constant along the minor radius. The hypothesis that was extracted to explain such a result is that the particle trajectories were wide enough to perform large radial excursions, hence connecting far regions of the plasma with different collisionalities and electric fields. The result of following collisionless trajectories of ions in TJ-II supported this hypothesis [11]. Nevertheless, an estimation of the effect of collisions was necessary to be sure that their effect is not able to change the transport regime that produces such a flat profile. In order to check this, we have considered the evolution of the temperature profile by

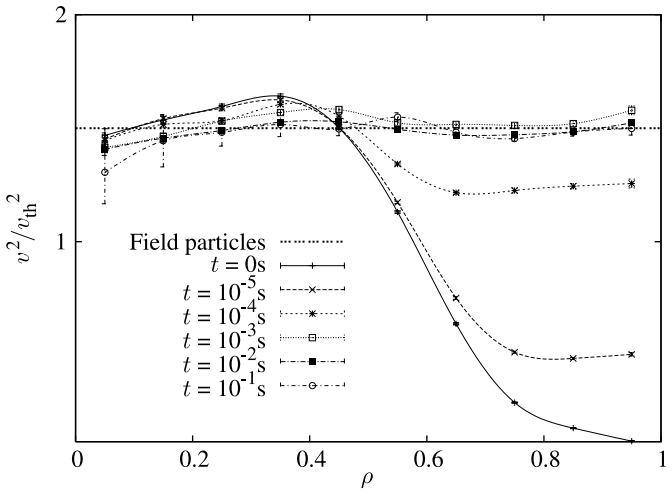

Figure 15. Kinetic energy profile as a function of the effective radius for several elapsed times from the trajectories launching. Note that even though the initial profile of the kinetic energy is chosen to be proportional to the particle density, the large radial excursions in the banana orbits and the collisions with the field particles produce a flat distribution at late times.

launching particles according to a temperature profile given by $T(\rho) = 100\,\mathrm{eV} \times (n(\rho)/n(0))$, considering the temperature profile of the field particles flat. The time evolution of such a temperature profile shows the tendency to flattening, reaching the equilibrium and overcoming the initial temperature inhomogeneity. The time scale of the flattening is $\sim 10^{-4}$–10^{-3} s, that is of the order of the thermalization time (see figure 15).

A different numerical experiment has been performed by launching the particles over a plasma whose ion background temperature profile is the same $T(\rho)$ defined in the previous paragraph. In this case, a tendency to flattening was observed up to $t \sim 10^{-3}$ s but, from this time on, the test particle temperature profile becomes more and more like that of the field particles. These two results imply that, in order to explain the dynamics of the temperature profiles, it would be necessary to let the test particles modify the background plasma. This non-linear computation has not been addressed in the present work.

7. Conclusions

The ion collisional transport is estimated for the TJ-II device by following the trajectories of a large number of particles ($\sim 10^6$) in the real geometry and in the presence of collisions and electric field. The magnetic configuration is simulated by using a grid in real space that does not assume the existence of nested flux surfaces, although in this work no islands or ergodic zones are considered.

This calculation method is valid for any collisional regime, avoiding the limitation of DKES calculations in the long mean free path regime in TJ-II, that produce large error bars. It also applies to the relation between collision and radial drift times, and thus can be employed in order to take into account global neoclassical effects. In particular, the ion–ion collision time in TJ-II varies from $\tau_c \approx 10^{-4}$ s in the centre of the plasma to $\tau_c \approx 10^{-3}$ s in the edge, to be compared with the average drift time, which is $\tau_r \approx 5 \times 10^{-3}$ s. Therefore, although the local ansatz is valid in the plasma centre, it can be questioned in the edge.

In this way, it is possible to estimate the collisional transport without any assumption on its local nature. We consider instead the influence of the whole particle history on transport. Hence, these calculations allow us to study the characteristics of the ion global transport. The initial distribution function of the particles is chosen to be off-equilibrium, which allows us to study both the transient behaviour under the effect of an electrostatic potential and the steady state behaviour of the ions. In particular, the stationary fluxes reach a stage of the simulation in which the error bars are still small enough to keep the results meaningful. Several phenomena have been observed that could not be discovered in the frame of the customary neoclassical transport calculations.

One of the main results of taking into account the actual particle trajectories that cannot be explained in the frame of the local ansatz is the monotonic increase of the heat and particle fluxes with minor radius, to be compared with those obtained using the standard calculation methods, that predict a non-monotonic behaviour with a maximum close to $\rho \approx 0.3$–0.4.

The global transport is observed to be non-diffusive. The time evolution of the average minor radius of all the particles $\langle\rho\rangle$ and its variance is the first feature of this characteristic. The latter shows diffusive behaviour in a time scale of 5×10^{-4} s, but is clearly non-diffusive for larger time scales, until the end of the evolution towards the minimum of the potential.

Despite the presence of collisions, the ion distribution function becomes non-Maxwellian due to both the selective losing of particles in different regions of velocity space and the presence of an electrostatic potential that provides an increase in kinetic energy when particles are closer to the minimum of the potential.

Finally, as an outstanding result, important asymmetries on transport appear. An up/down asymmetry is observed due to the characteristic TJ-II geometry and a non-homogeneous accumulation of particles is found on every magnetic surface. This latter fact is important to remove the customary assumption that the collisional transport can be approximated by a geometry in 1.5 dimensions. For particles confined in a device as complex as TJ-II in the low collisionality regime, it is clear that the assumption of having a large parallel transport that is able to homogenize the magnetic surfaces is not valid.

The method to investigate transport properties presented in this work is very well suited to the architecture of massively parallel computers and for grid computing, which makes it a promising tool for transport studies.

In a further work, we plan to study plasmas in a higher collisionality regime to find out which of these non-local features can still be found.

Acknowledgments

The authors are grateful to J M Reynolds for helping them to integrate the spatial grid in their C-code, as well as for providing figure A1. They acknowledge partial financial support from MEC (Spain), through research contract FIS2006-08533, European Commission through contracts, EGEE-II-031688 and int.eu.grid 031857, BSCH-UCM and CAM. J L Velasco is a DGA (Aragón, Spain) fellow.

Appendix A. The collision operator implementation

We shall use the collision operator developed in [13], based on previous results by Rosenbluth *et al* [27] (see also [22]). The basic assumption is that, in a nearly fully ionized plasma, the

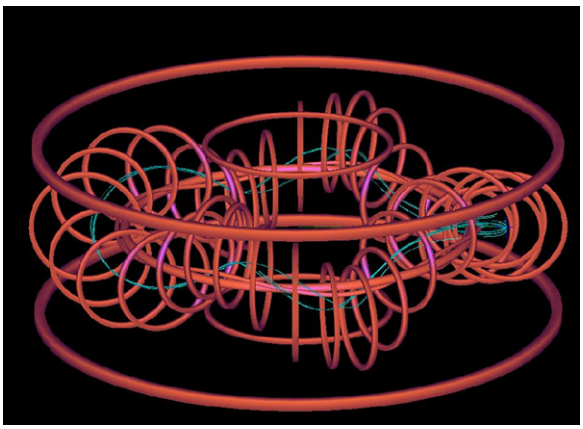

Figure A1. Scheme of the coils of the TJ-II. The thin lines represent the trajectories of 500 ions until $t = 10^{-4}$ s, starting from the same initial conditions.

(This figure is in colour only in the electronic version)

collisions with other charged particles dominate over those with neutrals. Due to the long-range nature of the Coulomb force, distant small angle collisions are much more probable than big angle scattering:

$$\mathcal{L}\hat{f} = \frac{\nu_{\mathrm{d}}}{2}\frac{\partial}{\partial\lambda}\left((1-\lambda^2)\frac{\partial\hat{f}}{\partial\lambda}\right) + \frac{1}{v^2}\frac{\partial}{\partial v}\left(v^2\nu_{\mathrm{E}}\left(v\hat{f} + \frac{T}{m}\frac{\partial\hat{f}}{\partial v}\right)\right), \tag{A.1}$$

where ν_{d} and ν_{E} are the deflection and the energy relaxation frequencies:

$$\nu_{\mathrm{d}} = \frac{3}{2}\sqrt{\frac{\pi}{2}}\nu_{B_i}\frac{\Phi(x)-\Psi(x)}{x^3}, \qquad \nu_{\mathrm{E}} = 3\sqrt{\frac{\pi}{2}}\nu_{B_i}\frac{\Psi(x)}{x}, \tag{A.2}$$

$$\nu_{B_i} = \frac{4}{3}\sqrt{\frac{\pi}{m_i}}\frac{e^4\, n_i \log\Lambda_i}{T_i^{3/2}}, \qquad \Lambda_i \approx \frac{3}{2}\sqrt{\frac{T_i^3}{\pi n_i}}\frac{1}{e^3}, \tag{A.3}$$

$$\Psi(x) = \frac{\Phi(x) - x\Phi'(x)}{2x^2}, \qquad \Phi(x) = \int_0^x \mathrm{d}y\,\frac{2}{\sqrt{\pi}}\mathrm{e}^{-y^2}. \tag{A.4}$$

Note that x is defined in equation (1), while ν_{B_i} is the Braginskii ion collision frequency, $\log\Lambda_i$ is the Coulomb logarithm for ions [28], n_i is the ion density (equal to that of the electrons), and the temperatures are now in electronvolt.

At first sight, equation (A.1) seems highly singular at $v = 0$, thus preventing us from interpreting it as a Fokker–Planck equation. However, the origin of the $1/v^2$ term is just in the choice made for the integration measure (for simplicity, we explicit only the v dependence):

$$\langle v^n\rangle = \int_0^\infty \mathrm{d}\,v\; 4\pi\, v^{n+2}\,\hat{f}(v). \tag{A.5}$$

Keeping in mind equation (1), we introduce a distribution function $f(x^2)$ (rather than $\hat{f}(v)$), such that

$$\langle v^n\rangle = \int_0^\infty \mathrm{d}\,x^2\,\left[\frac{2kTx^2}{m}\right]^{n/2} f(x^2). \tag{A.6}$$

With the choice for the integration measure in equation (A.6), equations (7) and (A.1) are equivalent to a standard Fokker–Planck equation:

$$\frac{\partial f}{\partial t} = -\vec{\nabla}_{r_{\rm GC}} \cdot (\vec{a}_{r_{\rm GC}} f) + \frac{\partial}{\partial \lambda}\left[-(a_\lambda + a_\lambda^{\rm Ito}) f + \frac{1}{2}\frac{\partial [b_\lambda^2 f]}{\partial \lambda}\right]$$
$$+\frac{\partial}{\partial x^2}\left[-(a_{x^2} + a_{x^2}^{\rm Ito}) f + \frac{1}{2}\frac{\partial [b_{x^2}^2 f]}{\partial x^2}\right], \tag{A.7}$$

$$a_\lambda^{\rm Ito} = -\lambda \nu_{\rm d}, \qquad b_\lambda = \sqrt{(1-\lambda^2)\nu_{\rm d}}, \tag{A.8}$$

$$a_{x^2}^{\rm Ito} = -2\nu_{\rm E}\left(x^2 - \frac{x}{\sqrt{\pi}}\frac{{\rm e}^{-x^2}}{\Psi(x)}\right), \qquad b_{x^2} = 2x\sqrt{\nu_{\rm E}}. \tag{A.9}$$

Note, however, that the drift terms $\vec{a}_{r_{\rm GC}}$, a_λ and a_{x^2} follow from the guiding-centre equations (2),(5) and (6), without any reference to collisions. Now, it is straightforward to write the corresponding (Itô-type) Langevin equations:

$$\frac{{\rm d}\vec{r}_{\rm GC}}{{\rm d}t} = \vec{a}_{r_{\rm GC}}, \tag{A.10}$$

$$\frac{{\rm d}\lambda}{{\rm d}t} = (a_\lambda + a_\lambda^{\rm Ito}) + \xi_\lambda\, b_\lambda^{\rm Ito}, \tag{A.11}$$

$$\frac{{\rm d}x^2}{{\rm d}t} = (a_{x^2} + a_{x^2}^{\rm Ito}) + \xi_{x^2}\, b_{x^2}^{\rm Ito}. \tag{A.12}$$

In order to construct the Stratonovich version of these Itô SDEs, we use (see, for example, [18])

$$a_{q_i}^{\rm Strat} = a_{q_i}^{\rm Ito} - \frac{1}{2}\sum_j \frac{\partial b_{q_i}^{\rm Ito}}{\partial q_j} b_{q_j}^{\rm Ito}, \quad b_{q_j}^{\rm Strat} = b_{q_j}^{\rm Ito}. \tag{A.13}$$

The sum must be made over all our coordinate space $q_k = \{\vec{r}_{\rm GC}, x^2, \lambda\}$. We obtain

$$\vec{a}_{r_{\rm GC}}^{\rm Strat} = 0 \quad (\text{note that } \vec{a}_{r_{\rm GC}}^{\rm Ito} = 0), \tag{A.14}$$

$$a_\lambda^{\rm Strat} = -\frac{1}{2}\lambda\nu_{\rm d} + \frac{1}{4}\sqrt{\nu_{\rm E}\nu_{\rm d}(1-\lambda^2)}\,\frac{5\Psi(x) - 3\Phi(x)}{x(\Psi(x) - \Phi(x))}, \tag{A.15}$$

$$a_{x^2}^{\rm Strat} = -2\nu_{\rm E}\left(x^2 - \frac{x}{\sqrt{\pi}}\frac{{\rm e}^{-x^2}}{\Psi(x)} + \frac{1}{2} + \frac{\Phi(x) - \Psi(x)(3+2x^2)}{4\Psi(x)}\right). \tag{A.16}$$

The resulting vector SDE is

$$\frac{{\rm d}\vec{r}_{\rm GC}}{{\rm d}t} = \vec{a}_{r_{\rm GC}}, \tag{A.17}$$

$$\frac{{\rm d}\lambda}{{\rm d}t} = (a_\lambda + a_\lambda^{\rm Strat}) + \xi_\lambda\, b_\lambda^{\rm Strat}, \tag{A.18}$$

$$\frac{{\rm d}x^2}{{\rm d}t} = (a_{x^2} + a_{x^2}^{\rm Strat}) + \xi_{x^2}\, b_{x^2}^{\rm Strat}. \tag{A.19}$$

Appendix B. The numerical algorithm

Two sources of inaccuracy must be controlled in the calculation of the SDEs. First of all, we are discretizing the trajectories with a finite time step Δt. This error can be always reduced

by increasing the numerical effort or using a better integration algorithm. More worrisome is the error induced by the spatial grid describing the magnetic configuration, because the mesh cannot be easily made finer. In order to get a quantitative estimate of the error induced by the spatial discretization, we have developed an alternative integration scheme. We will regard the numerical disagreement between the two schemes as a quantitative assessment of the discretization errors induced by the grid.

Appendix B.1. The integration scheme

As stated before, our minimum set of dynamical variables is formed by $\vec{r}_{\rm GC}$, the pitch, λ and the (normalized) kinetic energy, x^2. This leads to a set of SDEs, namely equations (A.10)–(A.12), that will be called x^2-scheme.

Equivalently, the chosen set of dynamical variables could have been $\vec{r}_{\rm GC}$, λ and the normalized total (i.e. kinetic plus potential) energy:

$$\varepsilon = x^2 + \frac{e\Phi}{kT}. \tag{B.1}$$

Since the Jacobian of the change of variables from $\{\vec{r}_{\rm GC}, x^2, \lambda\}$ to $\{\vec{r}_{\rm GC}, \varepsilon, \lambda\}$ is a numerical constant, it is straightforward to obtain the SDEs of the ε-scheme:

$$\frac{{\rm d}\varepsilon}{{\rm d}t} = (a_\varepsilon + a_\varepsilon^{\rm Strat}) + \xi_\varepsilon\, b_\varepsilon, \tag{B.2}$$

$$a_\varepsilon = 0, \qquad a_\varepsilon^{\rm Strat} = a_{x^2}^{\rm Strat}, \qquad b_\varepsilon = b_{x^2}. \tag{B.3}$$

The kinetic energy can be quoted at each step from equation (B.1). The Itô version can be obtained using (A.13).

The two integration schemes should yield equivalent results, up to systematic errors induced by the spatial discretization.

Appendix B.2. The integration algorithm

Our task is to solve a set of vector stochastic differential equations. The Gaussian noise, with uncorrelated components, is multiplicative. For each component q_α, we have

$$\frac{{\rm d}q^\alpha}{{\rm d}t} = f^\alpha(q^\kappa) + g^\alpha(q^\kappa)\xi^\alpha(t), \tag{B.4}$$

$$\langle \xi(t)^\alpha \rangle = 0, \qquad \langle \xi(t)^\alpha \xi(t')^\beta \rangle = \delta(t-t')\delta^{\alpha,\beta}. \tag{B.5}$$

Note that, for the sake of brevity, we introduce the following notation:

$$f^\alpha \equiv a_\alpha + a_\alpha^{\rm col}, \qquad g^\alpha \equiv b_\alpha. \tag{B.6}$$

We have discarded the Euler algorithm [18] because of its poor convergence. Indeed, its order of weak convergence (i.e. the order of convergence for mean values) is only 1, which is not enough for the long simulations that we are performing. Thus, we need to resort to a higher order algorithm, but not too high because of the spatial grid. We have considered three algorithms of the second-order convergence in the deterministic part, but of only first order of weak convergence in the presence of multiplicative Gaussian noises. Namely, we checked a direct Itô generalization of the Heun algorithm [29], a two-stage Itô algorithm by Klauder and Petersen [23] and a two-stage Stratonovich algorithm by Kloeden and Pearson [24]. The latter type of algorithm has been claimed to be of second weak order convergence, but this is not true for the case with several multiplicative Gaussian noises [18]. However, we numerically find that the linear term is exceedingly small.

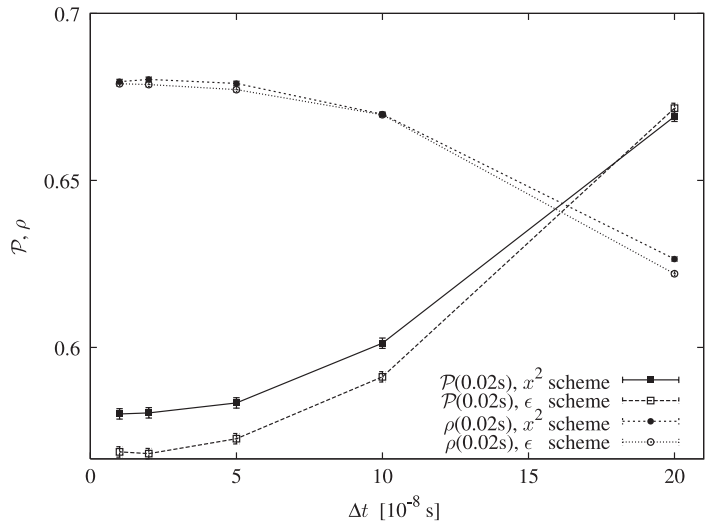

Figure B1. Persistence (i.e. fraction of surviving trajectories after at considered time) and $\langle\rho\rangle$ for particles in the plasma at time $t = 0.02$ s as a function of the time-step Δt for the two integration schemes for the Kloeden–Pearson algorithm (different algorithms yield statistically compatible results, even at finite Δt).

The equations for our final choice (Kloeden-Pearson) are

$$q^\alpha_{\mathrm{d}t} = q^\alpha_0 + \frac{1}{2}(f^\alpha_0 + f^\alpha_1)\delta t + \frac{1}{2}(g^\alpha_0 + g^\alpha_1)\sqrt{\delta t}\,Y^\alpha, \tag{B.7}$$

$$q^\alpha_1 = q^\alpha_0 + f^\alpha_0 h + g^\alpha_0\sqrt{\delta t}\,Y^\alpha, \tag{B.8}$$

where we denote

$$q^\alpha_0 \equiv q^\alpha(t=0), \qquad f^\alpha_0 \equiv f^\alpha(q^\kappa_0), \qquad g^\alpha_0 \equiv g^\alpha(q^\kappa_0), \tag{B.9}$$

and Y^α will be independent Gaussian distributed random numbers of zero mean and unit variance.

Appendix B.3. Choice of scheme, algorithm and integration step

We have made a study of convergence of all these algorithms and schemes in our system, with Δt between 2×10^{-7} s and 1×10^{-8} s. For every case (a total of 6 independent simulations) we have calculated 10^5 trajectories, which means 10% of the total statistics in our final results. We have measured several quantities as an average of the whole of particles at a finite time (after $\sim 10^5$ to 10^6 integration steps). We observe that the choice of algorithm is immaterial. We plot in figure B1 the results for the Kloeden–Pearson algorithm. Note that, although the weak convergence should be linear in Δt, it turns out to be quadratic, as we said before (consider that we are working in a low collisionality regime). In the production runs, we have stuck to the thoroughly studied Kloeden–Pearson algorithm. For our statistical errors in all observables, we can safely set $\Delta t = 2\times10^{-8}$ s.

However, we find differences between the $\Delta t \to 0$ limits of the x^2-scheme and the ε-scheme. In figure B1 we show the convergence to $\Delta t \to 0$ of a typical observable, $\langle\rho\rangle$, and the worst case, the persistence (see section 4). To quantify the discrepancy, we can fit the late decay of the persistence versus time to the functional form $\mathcal{P}(t) \sim e^{-t/\tau}$. We obtain

$$\tau_\varepsilon = 0.0277(3)\ \mathrm{s}, \qquad \tau_{x^2} = 0.0286(1)\ \mathrm{s}, \tag{B.10}$$

which differ about 3%. Thus, this systematic error is of the same order as the one arising from our choice of criterion for ending a trajectory (see section 4).

Appendix C. Calculation of fluxes

Let us consider the ion flux integral, defined in equation (15)

$$\Gamma(\rho) = \int_S \int_0^\infty \mathrm{d}\, x^2 \int_{-1}^{1} \mathrm{d}\,\lambda\; f(\vec{r}_{\mathrm{GC}}, \lambda, x^2)\; \vec{u} \cdot \mathrm{d}\vec{S}. \tag{C.1}$$

A Monte Carlo method allows to calculate volume integrals. In order to compute a surface integral, we transform the surface integral over S in a volume integral over a radial corona of width $\Delta\rho = 0.1$:

$$\Gamma(\rho) \approx \frac{1}{\Delta\rho} \int_{(S\times\Delta\rho)} \int_0^\infty \mathrm{d}\, x^2 \int_{-1}^{1} \mathrm{d}\,\lambda\; f(\vec{r}_{\mathrm{GC}}, \lambda, x^2)\; (\vec{u} \cdot \mathrm{d}\vec{S})\mathrm{d}\rho. \tag{C.2}$$

Now, our distribution function is

$$f(\vec{r}_{\mathrm{GC}}, \lambda, x^2) = \langle \sum_{i\in\text{plasma}} \delta^{(3)}(\vec{r}_i - \vec{r})\delta(x_i^2 - x^2)\delta(\lambda_i - \lambda)\rangle. \tag{C.3}$$

We use the fact that $\delta^{(3)}(\vec{r}_i - \vec{r}) = |\vec{\nabla}\rho|\delta(\rho_i - \rho)\delta^{(2)}(\vec{S}_i - \vec{S})$, which leads to

$$\Gamma(\rho) \approx \frac{1}{\Delta\rho} \sum_{i\in(S\times\Delta\rho)} (\vec{u} \cdot \vec{\nabla}\rho)_i. \tag{C.4}$$

Thus, at a given time, the flux is obtained just adding, for all ions that are in a radial corona, the guiding-centre velocity times the gradient of the magnetic coordinate ρ. Note that the sum is made over the whole velocity space. We then normalize by the total number of ions in the plasma. The radial energy flux is calculated in a similar way, by adding for all the particles the kinetic energy, $\frac{1}{2}mv^2$, times the guiding-centre velocity of the velocity times the gradient of the magnetic coordinate ρ.

Consider now the toroidal flux defined in equation (17):

$$\Gamma_\phi(\rho) = \int_{S_{\mathrm{C}}} \int_0^\infty \mathrm{d}\, x^2 \int_{-1}^{1} \mathrm{d}\,\lambda\; f(\vec{r}_{\mathrm{GC}}, \lambda, x^2)\; u_\phi \mathrm{d}S. \tag{C.5}$$

The same procedure as before leads to

$$\Gamma_\phi(\rho) = \lim_{\Delta\phi\to 0} \frac{1}{\Delta\phi} \sum_{i\in(S_{\mathrm{C}}\times\Delta\phi)} (u_\phi)_i. \tag{C.6}$$

Averaging in the toroidal angle we obtain

$$\langle\Gamma_\phi\rangle(\rho) = \frac{1}{2\pi} \sum_{i\in S_{\mathrm{C}}\times 2\pi} (u_\phi)_i = \frac{1}{2\pi} n(S_{\mathrm{C}})\langle u_\phi\rangle_{S_{\mathrm{C}}}, \tag{C.7}$$

$n(S_{\mathrm{C}})$ is the amount of ions that are in the corona S_{C}, and the average is made over these particles.

Another consideration can be done in order to make more accurate the flux calculation. Given a selected time t_0, there is no relevant evolution of the system between $0.9t_0$ and $1.1t_0$ (see, for example, figure 10 or 9, note the logarithmic scale). Then, one can consider all the measurements in the interval to belong to the same time $t = t_0$, thus increasing significantly the statistics. Obviously, this method will actually reduce the error bars if the measured data are statistically independent. For this to be true, ions should move significant during the time interval. In our system (see figure 7) this starts to happen from $\sim 10^{-4}$ s. As a consequence, largely reduced error bars are obtained for $t > 10^{-3}$ s.

References

[1] Lotz W, Merkel P, Nürenberg J and Strumberger E 1992 *Plasma Phys. Control. Fusion* **34** 1037
[2] Shasharina S G and Cary J R 1993 *Nucl. Fusion* **33** 648
[3] Kurki-Suonio T *et al* 2002 *Nucl. Fusion* **42** 725
[4] Kiviniemi T *et al* 2005 *32nd EPS Plasma Physics Conf. (Tarragona, Spain)*
[5] Wobig H 1999 *Plasma Phys. Control. Fusion* **41** A159
[6] Christiansen J P and Connor J W 2004 *Plasma Phys. Control. Fusion* **46** 1537
[7] Alejaldre C *et al* 1990 *Fusion Technol.* **17** 131
[8] Hirshman S P and Whiston J C 1983 *Phys. Fluids* **26** 3553
[9] Solano E, Rome J A and Hirshman S P 1988 *Nucl. Fusion* **28** 157
[10] Tribaldos V 2001 *Phys. Plasmas* **8** 1229
[11] Castejón F *et al* 2006 *Fusion Sci. Technol.* **50** 412
[12] Tribaldos V and Guasp J 2005 *Plasma Phys. Control. Fusion* **47** 545
[13] Boozer A and Kuo-Petravic G 1981 *Plasma Phys.* **24** 851
[14] Lotz W, Nürenberg J and Schlüter A 1987 *J. Comput. Phys.* **73** 73
[15] Fontdecaba J M *et al* 2004 *Fusion Sci. Technol.* **46** 271
[16] Guasp J and Liniers M 2000 *Nucl. Fusion* **40** 397
[17] Guasp J and Liniers M 2000 *Nucl. Fusion* **40** 411
[18] Kloeden P E and Platen E 1992 *Numerical Solution of Stochastic Differential Equations* (Berlin: Springer)
[19] Arnold L 1974 *Stochastic Differential Equations: Theory and Applications* (NewYork: Wiley)
[20] Mannella R 2000 A gentle introduction to the integration of stochastic differential equations *Stochastic Processes in Physics, Chemistry, and Biology* ed J A Freund and T Poshel (Berlin: Springer) p 353
[21] Van Kampen N G 1981 *Stochastic Processes in Physics and Chemistry* (Amsterdam: Elsevier)
[22] Chen T S 1988 A General form of the Coulomb scattering operators for Monte Carlo simulations and a note on the guiding center equations *Different Magnetic Coordinate Conventions* IPP 0/50 (Max-Planck-Institut für Plasmaphysik)
[23] Klauder J R and Petersen W P 1989 *Numerical Integration of Multiplicative-Noise Stochastic Differential equations* (AT&T Bell Labs Preprint)
[24] Kloeden P E and Pearson R A 1977 The numerical solution of stochastic differential equations *J. Aust. Math. Soc.* B **20** 8–12
[25] García-Cortés I *et al* 2002 *Plasma Phys. Control. Fusion* **44** 1639
[26] Ochando M A *et al* 2006 *Fusion Sci. Technol.* **50** 313
[27] Rosenbluth M N, MacDonald W and Judd D 1957 *Phys. Rev.* **107** 1
[28] Skupsky S 1987 *Phys. Rev.* A **36** 5701
[29] Velasco J L 2006 *Doctoral Thesis* University of Zaragoza (in preparation)